Journal of Molecular Graphics and Modelling 124 (2023) 108576

Contents lists available at ScienceDirect

Journal of Molecular Graphics and Modelling

journal homepage: www.elsevier.com/locate/jmgm

Divalent ions as mediators of carbonylation in cardiac myosin binding protein C

Christina Bergonzo [a,*], Baikuntha Aryal [b], V. Ashutosh Rao [b]

[a] Institute for Bioscience and Biotechnology Research, National Institute of Standards and Technology, the University of Maryland, 9600 Gudelsky Way, Rockville, MD, 20850, USA

[b] Laboratory of Applied Biochemistry, Division of Biotechnology Review and Research III, Office of Biotechnology Products, Office of Pharmaceutical Quality, Center for Drug Evaluation and Research, U.S. Food and Drug Administration, Silver Spring, MD, USA

ARTICLE INFO

Keywords:
Protein carbonylation
Metal ion-induced ROS
Molecular dynamics
cMyBP-C

ABSTRACT

The dosing and efficacy of chemotherapeutic drugs can be limited by toxicity caused by off-pathway reactions. One hypothesis for how such toxicity arises is via metal-catalyzed oxidative damage of cardiac myosin binding protein C (cMyBP-C) found in cardiac tissue. Previous research indicates that metal ion mediated reactive oxygen species induce high levels of protein carbonylation, changing the structure and function of this protein. In this work, we use long timescale all-atom molecular dynamics simulations to investigate the ion environment surrounding the C0 and C1 subunits of cMyBP-C responsible for actin binding. We show that divalent cations are co-localized with protein carbonylation-prone amino acid residues and that carbonylation of these residues can lead to site-specific interruption to the actin-cMyBP-C binding.

1. Introduction

The chemotherapeutic drug Doxorubicin, a common and effective anticancer treatment, has dose-dependent cardiotoxic side effects in 10%–30% of treated patients. Previous work has found that cardiac myosin binding protein C (cMyBP-C), a 140 kDa protein required for regulating cardiac muscle contraction [1], is selectively carbonylated in vitro during chemotherapeutic drug-induced metal-catalyzed oxidative stress [2]. Carbonylation is a type of protein oxidation that results in irreversible modifications of amino acid residues proline, arginine, lysine, and threonine [3,4]. Excessive protein carbonylation may alter structural and functional activities and leads to aggregation or degradation of the altered protein [5]. In earlier studies, carbonyl modification leading to degradation of cMyBP-C was found to be an indicator of cardiotoxicity. The prevention of cMyBP-C carbonylation and degradation resulted from the addition of an iron (Fe^{2+}) chelator, linking a decrease in metal-catalyzed oxidation with cardioprotection [2].

While previous work showed that the cMyBP-C protein is carbonylated during metal-catalyzed oxidative stress [2], mass spectrometric data indicating the positions of modified residues was not reported. Carbonylation of cMyBP-C lowers its affinity for actin [2], implicating changes are localized in the actin binding region of cMyBP-C, specifically the C0-linker-C1 subunits. In addition to carbonylation, other post translational modifications, including serine phosphorylation, modulate cMyBP-C's interactions with binding partners and are localized to the same region [6–8]. Site-specific protein carbonylation is difficult to predict accurately based on sequence alone [9], though general rules exist: prolines exhibit the highest susceptibility to carbonylation, although they have low incidence in proteins; whereas lysine is the least likely residue to be carbonylated but is more abundant [9]. Several sequence-based and other predictors have been developed [3,9–13], though a more robust approach would take into account the 3-dimensional structure and dynamics of proteins.

cMyBP-C is a multidomain protein consisting of a chain of 11 subunits, numbered C0 through C10. Each subunit contains roughly 110 amino acids, which have been determined both from X-ray crystallography and nuclear magnetic resonance (NMR) modeling [14–21]. Fig. 1 shows the sequence comparison of the C0 and C1 subunits obtained from deposited PDB structures 2K1M [20] and 3CX2 [21], as well as the structural overlap between these subunits illustrating their immunoglobulin (Ig) like fold. The C0-linker-C1 region binds cooperatively to the thin filament [22]: actin interacts with C0 and influences C1 binding to tropomyosin (Tm). Both C0 and C1 have "actin-binding" faces, identified through NMR chemical shift data from titration with actin. The residues involved in the actin-binding faces include 31, 42, 49, 77, 80, 81, 83, 90 for C0 and 191, 197, 198, 202, 230, 237, 242 for C1. C1

* Corresponding author.
E-mail address: christina.bergonzo@nist.gov (C. Bergonzo).

https://doi.org/10.1016/j.jmgm.2023.108576
Received 23 May 2023; Received in revised form 12 July 2023; Accepted 27 July 2023
Available online 28 July 2023
1093-3263/Published by Elsevier Inc.

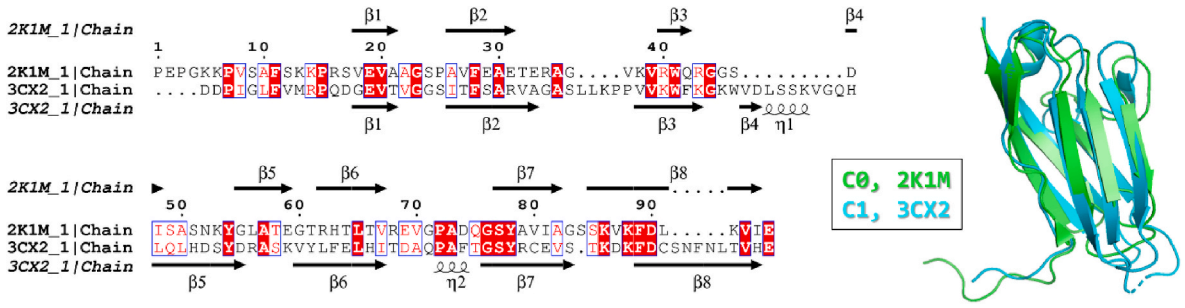

Fig. 1. Left: Clustal alignment of C0 and C1 subunit sequences and their secondary structures. Identical residues are highlighted in red, residues with a similarity score above 0.7 are shown as red letters. Right: Overlap of 2K1M (green) and 3CX2 (cyan) structures of C0 and C1 subunits, respectively. RMSD between the two structures is 1.74 Å. (For interpretation of the references to color in this figure legend, the reader is referred to the Web version of this article.)

binds the Tm domain with the RASK loop, specifically residues R215 and K218. Mutations of both R215 and K218 to Glu inhibit binding (via ATP hydrolysis rate measurements) at varying cMyBP-C concentrations [22]. The importance of these residues was structurally confirmed through cryoelectron microscopy (cryo-EM) imaging of the full thin filament by Risi et al. [22].

In the deposited cryo-EM models, the C1 subunit consistently adopts a "side mode" binding conformation as observed in all C0C1 co-crystallized sets. While all reported structures (6CXI, 6CXJ, 6G2T) show C1 in the same conformation, they have either conformation 1 or 2 of C0 or C0 is absent, respectively [22]. Residues identified by NMR chemical shift analysis and mentioned above are oriented towards actin in the 6CXI structure [23]. Together, these pieces of structural data begin to paint a picture of the specific interactions in the thin filament which may be disrupted by reactive oxygen species (ROS) induced carbonylation.

To address the complicated interplay of divalent metal ions which induce ROS, the ionic environment around the C0 and C1 subunit structures, and the relative propensities for carbonylation of each protein subunit, we used all-atom molecular dynamics simulations. Molecular dynamics simulations were run for 5 μs to converge solvated Cu^{2+} and Fe^{2+} ion distributions around each C0 and C1 protein subunit. We analyzed the ion distribution around the protein residues [24]. Despite high structure homology, differences in sequence drive different ion association events. For C1, most interactions are on the solvent exposed face, though some persist along the actin-binding region. For C0, Cu^{2+} interactions are in general more diffuse, but where we do see high fraction occupancy, it is also on the solvent exposed face of C0. These results were modeled on the thin filament cryo-EM models to uncover the mechanism of divalent ion mediated ROS-induced carbonylation.

2. Materials and methods

The C0 and C1 subunit starting coordinates were taken from PDBs 2K1M [20] and 3CX2 [21], respectively. The C1 subunit was missing density in the Ser32 residue, and loop coordinates A29-P36 from another C1 PDB structure model determined by NMR (2AVG [16]) was fitted to the 3CX2 structure and minimized. The resulting C0 and C1 structures were built in tLEaP using the recommended Amber protein force field ff19SB [25] and SPC/E water [26], with Li and Merz divalent ion parameters for Cu^{2+} and Fe^{2+} (consensus set) [27]. A constant protonation state was assigned to each residue based on a pH of 7.0. A buffer of 10.0 Å from the edge of the solute to the edge of the truncated octahedral box was used, and one Na^{+} ion was added to neutralize the protein's charge. An additional 23 Cu^{2+}/Fe^{2+} ions and 46 Cl^{-} ions were added resulting in a 100 mmol/L ion concentration. Ions were randomized by swapping with water molecules 6 Å from the solute protein and 4 Å from each other, using eight different random seeds to generate eight starting coordinate sets for each ion (Cu^{2+}/Fe^{2+}) and each protein (C0 and C1) (8 replicates per ion and protein pair, 32 total simulations).

Each system was minimized and equilibrated using AmberEquil and previously published inputs [28]. A ten-step protocol as described was used, combining successive rounds of minimization and equilibration with decreasing positional restraints, in both isobaric-isothermal (NPT) and canonical (NVT) ensembles. Hydrogen mass repartitioning was used, setting the mass of hydrogen atoms to 3.024 Da and decreasing the mass of the heavy atoms to which the hydrogen atom is bonded by the same amount [29]. In addition, SHAKE was used, which allowed a 4 fs timestep for simulations [30]. Each of the eight simulations per protein and ion condition was run for 5 μs in an NPT ensemble, totaling eight replicate simulations per ion and protein pair, each run for 5 μs, accumulating 40 μs of trajectory data. Pressure was regulated using a Monte Carlo barostat [31] at 1 atm, and temperature was set to 300 K and regulated using a Langevin thermostat [32], with a collision frequency of 5 ps^{-1} and a random seed set to prevent synchronization artifacts [33]. A direct space cutoff for particle mesh Ewald [34] of 9.0 Å was used. Simulations were run on NVIDIA Titan-XP GPUs using pmemd.cuda.MPI [35]. Analysis was performed using Cpptraj [24], and included root mean square deviation, root mean square fluctuation, grid, hbond, and native contacts analyses (included as Supporting Scripts).

To map ion grid density onto subunits of the multidomain thin filament complex, a two-step analysis protocol in Cpptraj was used. In the first Cpptraj pass, a single 5 μs trajectory for a given protein subunit and ion type was used to define the bounds of the 3D grid needed to cover the protein. After calculating the bounds in Angstroms and adding an 8 Å offset, the number of bins in each dimension (x, y, z) based on a 0.5 Å histogram bin width was collected from the Cpptraj output. In the second Cpptraj pass, all trajectory information per protein subunit per ion type was read in, along with the thin filament cryo-EM structure as a reference. A 'for' loop was established to grid the ions to the six subunits of the larger assembly, and output grids for each subunit were saved. An in-depth tutorial for mapping ion grid density onto subunits of larger structures is provided at (https://amberhub.chpc.utah.edu/mapping-ion-density/), and the two analysis scripts are included as Supporting Scripts.

Visualization was performed using PyMol [36] and Visual Molecular Dynamics (VMD) [37], and sequence alignment was performed using Clustal [38] and espript [39]. Thin filament structures with C0 and C1 subunit grids in dx format, and PDBs with relative contact strength in the B-factor column are available on GitHub (https://github.com/cbergonzo/cMyBP-C).

3. Results

3.1. Calculation of divalent ion density around C0 and C1 subunits

Simulations of divalent ions around the C0 and C1 subunits show different localization, which are attributed to sequence-specific

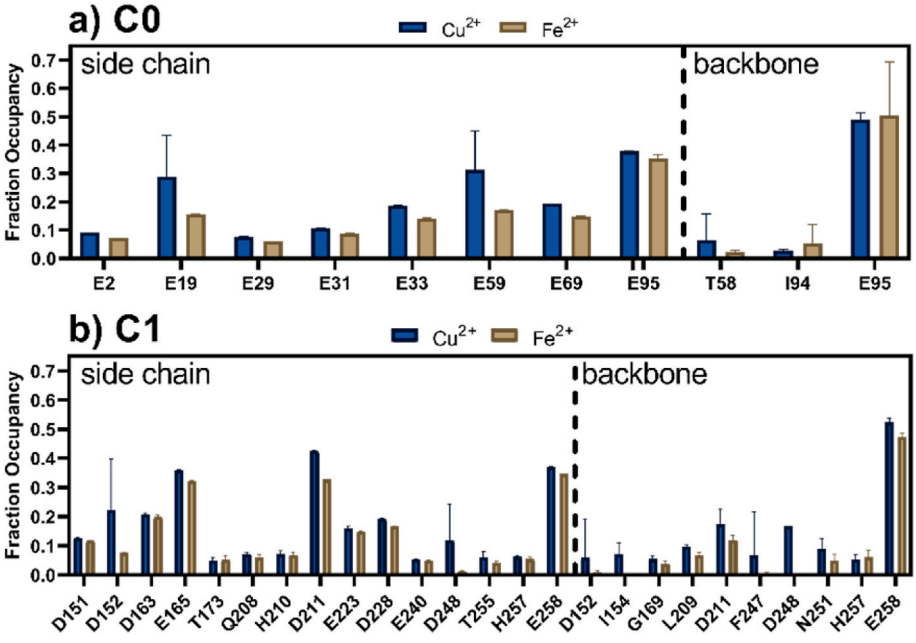

Fig. 2. Cu^{2+} (blue) and Fe^{2+} (brown) ion occupancies for a) C0 and b) C1 subunits, separated by side chain (left) and backbone (right) atoms. Occupancies over 0.05 (equivalent to 5%) are shown. Average values and standard deviations are calculated from eight 5 μs simulations for C0 and C1, with Cu^{2+} or Fe^{2+}. (For interpretation of the references to color in this figure legend, the reader is referred to the Web version of this article.)

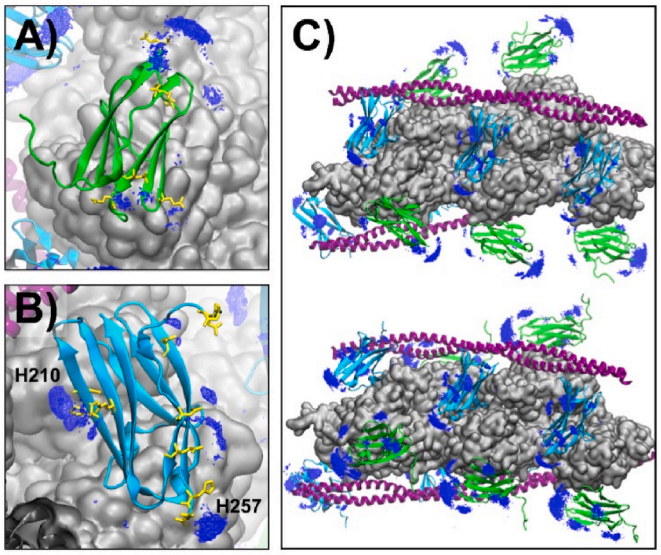

Fig. 3. Cu^{2+} density 10 × bulk concentration, shown as blue grid, overlapped with models of the thin filament from PDBs 6cxi and 6cxj. Yellow residues are those that have over 0.10 occupancy reported in Fig. 2. A) C0 (green) density; B) C1 (cyan) density; C) Thin filament models (6CXI top and 6CXJ bottom) with C0 (green) shown in different poses. Actin is shown as a silver surface, and tropomyosin is shown as purple helices.
Carbonylation prediction in C0 and C1. (For interpretation of the references to color in this figure legend, the reader is referred to the Web version of this article.)

interactions. Although the subunits share the same overall immunoglobulin-like fold, they have different ion environments due to their differing amino acid sequences. Fig. 2 shows the ion-protein residue interactions which exist for >5% of the simulated frames, where averages and standard deviations are reported over the eight independent 5 μs simulations per ion-protein pair. Interactions between protein atoms and ions were determined by a distance cutoff of 4.75 Å to account for interactions which occur through the ion's hydration shell. For some ion-residue pairs, this density is highly converged across eight simulations, noted by small error bars. For other ion-residue pairs, such as D152, error bars are larger, reflecting ion chelating events after the loss of an inner shell water molecule, which occur in single simulations are irreversible on the simulated timescales. In the C0 subunit, the highest density is localized around mainly glutamic acid residues. The C1 subunit simulations show Cu^{2+} density interacting with charged aspartic acid and glutamic acid residues, with some density around histidine residues H210 sidechain and H257 backbone and sidechain. Additionally, both subunits show high occupancy for C-terminal residues (solvent exposed oxygens) that are an artifact of truncating the subunit, because in vivo these residues are connected to other protein regions (i.e., they are not independent monomers). Both C0 and C1 subunits show some interaction of Cu^{2+}/Fe^{2+} with threonine residues, which are susceptible to carbonylation, in both the sidechain and backbone atoms, including T58, T173, and T255 (Fig. 2).

3.2. Mapping ion density onto the thin filament

Ion density around the individual C0 and C1 subunits and mapped onto all subunits along the thin filament cryo-EM model are shown in Fig. 3. Panels A and B in Fig. 3 show close up views of the C0 and C1 subunits, with Cu^{2+} ion density 10 × bulk ion concentration illustrated as a blue grid. Yellow licorice representation is used to highlight residues which measure over 0.10 fraction occupancy for the simulated trajectory frames, per Fig. 2. Actin is represented as silver surface representation, and tropomyosin is shown as purple helices. In the individual subunits, ion density around charged, acidic/basic residues is obvious for both C0 and C1, and as well as the significant density around the histidine residues H210 and H257 in Fig. 3B for C1. The C0 subunit has more diffuse density. The C1 subunit has comparatively more clear association sites, including sites adjacent to the actin binding face (and ordered, in part, by the histidine residues). A comparison between association sites of C0 and C1 proteins with Fe^{2+} and Cu^{2+} density is displayed using orientation graphs in Supporting Fig. 1. Although simulations were not run in the context of the thin filament, and only were run on the individual monomers, there is good agreement with ion

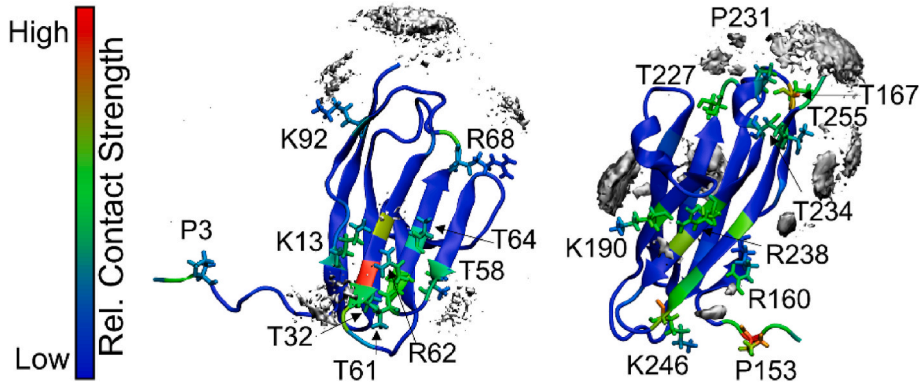

Fig. 4. C0 (left) and C1 (right) subunits with Cu^{2+} ion density colored by relative contact 'hotspot' for carbonylation by metal induced ROS. Selected carbonylation sites (R, K, P, are shown as licorice representation. Highest relative contact strength is shown in red and low relative contact strength is shown in blue. (For interpretation of the references to color in this figure legend, the reader is referred to the Web version of this article.)

Table 1
Carbonylation sites (R,K,T,P) in C0 and C1 subunits ranked by relative contact strength to metal ion coordinating residues.

C0 Residues	Rel. Contact Strength (out of 100)		C1 Residues	Rel. Contact Strength (out of 100)	
	Cu^{2+}	Fe^{2+}		Cu^{2+}	Fe^{2+}
R62	42.61	43.36	P153	72.18	72.63
T32	34.58	34.63	T167	58.18	62.55
T61	34.11	35.18	R238	48.74	47.95
K13	30.24	30.04	T227	46.64	48.17
T64	27.97	28.18	K246	43.08	47.43
T58	25.40	25.16	K190	36.50	33.44
P3	20.51	19.98	P231	29.48	26.99
K92	18.18	18.36	T234	28.76	27.77
P1	17.05	16.82	T255	28.02	27.70
R34	15.80	15.89	R160	25.08	25.21
P15	13.41	13.48	P161	16.97	17.60
R68	11.92	12.06	T243	16.84	19.91
K53	11.07	10.75	R177	12.65	12.11
P25	10.55	10.62			

density occupying the solvent-exposed faces of both C0 and C1.

To put divalent ion density for these subunits in the context of the 'complete' thin filament (Fig. 3C), both C0+C1 3D reconstructions from cryo-EM are shown. In each representation, the C1 subunit is in the same relative orientation with respect to the actin and tropomyosin. The C0 subunit changes orientation in each reported thin filament structure. Notable observations from these models include ion density on solvent-exposed loops of C0, while C1 ion density is localized to potentially interrupt actin binding.

To assign hot spots for metal ion induced carbonylation, the amino acid residues that can be carbonylated (R, K, P, T) within an interaction cutoff of 5 Å for Cu^{2+} associating residues were identified. This cutoff assumes that residue carbonylation propensity is related to metal ion proximity. The structures of C0 and C1 shown below in Fig. 4 are colored by relative contact strength (additive number of interactions) between Cu^{2+} associating residues (determined by fraction occupancy values over 0.05) and RKPT residues. For C0, the residues with the highest relative contact strength include T61, T32, and R62, with the rest listed in Table 1 (contact strength for all R, K, P, T residues is shown in Supporting Table 1). For C1, the residues with the highest relative contact strength include P153, T167, R238, K246, T227 and those listed in Table 1 (contact strength for all residues is shown in Supporting Table 1). Some overlap between the ion density and R, K, P, T residues is obvious in Fig. 4. There are also areas of each protein with some ion density but low contact which are not adjacent to any R, K, P, T residues.

4. Discussion

The work presented here yields structural insights into metal-catalyzed and ROS-mediated carbonylation of the cardiac MyBP-C protein. We also probe sequence specific differences in carbonylation propensity that arise between structurally homologous protein subunits. The Ig-like folds of the C0 and C1 domains are interesting examples of structural homologs with functional differences. The C0 subunit, specific to the cMyBP-C, primarily interacts with actin, while the C1 subunit interacts with the tropomyosin through the RASK loop, in addition to several residues that interact with actin. The overall folds, shown in Fig. 1, are similar but the sequences are variable in almost all regions (including loops and β-sheets). Variations in the sequence-specific susceptibility to carbonylation is likely to impact different binding and biological functions of cMyBP-C protein, and reinforces the conclusions from Risi et al. that these N-terminal subunits are responsible for different functions in thin filament binding and activation [22].

The predicted density of divalent Cu^{2+} and Fe^{2+} ions around the C0 and C1 subunits (Fig. 2) is localized around the oxygen atoms of aspartic and glutamic acid sidechains, in addition to the nitrogen atom in singly protonated histidine in the C1 subunit. This is expected behavior for divalent ions associating with proteins [40,41]. Of particular interest are ion association events with residues that are carbonylated: proline, threonine, arginine, and lysine. Significant ion density is associated with some threonine residues during the simulations (shown in Fig. 2, T58 in C0, T173 and T255 in C1).

To integrate the divalent ion association probabilities, carbonylation-susceptible amino acids, and 3-dimensional orientation of all players in the thin filament, the ion densities were mapped onto the C0 and C1 subunits from cryo-EM based models of the thin filament (Fig. 3). The C0C1 protein orientations allow for ion association with the solvent-exposed surfaces. Although most of the ion density is around flexible loop regions of both C0 and C1, there is significant density surrounding the histidine residues on the beta sheet of C1 close to the actin-binding interface.

Identification of hot-spots for carbonylation based on structure, i.e., proximity of carbonylation-prone R, K, P, T residues close to divalent-ion association points, was analyzed for C0 and C1 and reported in Fig. 4. Hot spots report the residue carbonylation propensity with respect to the residue's proximity to redox active metal ions. Current carbonylation prediction tools are limited to sequence and do not include higher order structure [42]. In contrast, the results presented here consider structure and dynamics in addition to sequence, leading to a more robust means to predict carbonylation hot spots.

The tropomyosin and actin binding residues in the C1 protein, detailed in Risi et al. (RASK loop of C1 interacts with Tm in cryo-EM based models) [22] and Lu et al. (chemical shift changes during

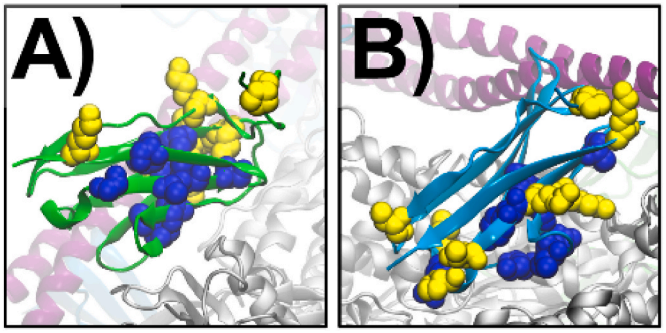

Fig. 5. Summary of MD predicted carbonylation and NMR-validated actin binding residues mapped onto 6CXI cryo-EM structure. Purple helices are tropomyosin, silver proteins are actin. A) C0 (green) and B) C1 (cyan) protein subunits are shown in cartoon representation. Blue residues are most perturbed chemical shifts upon actin binding (from Ref. [23]), and yellow are the top eight most susceptible carbonylation sites in Table 1. Overlap between these regions exists in the C1 subunit. (For interpretation of the references to color in this figure legend, the reader is referred to the Web version of this article.)

^{15}N-^{1}H HSQC NMR upon actin titration) [23], respectively, show some overlap with noted carbonylation-susceptible "hot spots" (Fig. 5B). The C0 residues which are predicted carbonylation "hot spots" do not show good agreement with actin binding residues determined by NMR (Fig. 5A). However, the ion density was overall more diffuse around C0, and additionally the C0 subunit exhibits multiple binding modes in the cryo-EM data. It is reasonable to posit that the carbonylation of susceptible residues interferes with actin binding based on the C1 subunit, since the predicted sites overlap with residues that have been experimentally determined to bind actin. Due to the conformational plasticity of the C0 subunit, the lack of overlap seems reasonable. These findings also agree with previous experimental evidence of significantly reduced actin binding by carbonylated cMyBP-C [2].

5. Conclusion

Although previous work has shown that ROS-induced carbonylation of the cMyBP-C protein is associated with reduced actin-binding and cardiotoxicity, interactions between transition metal ions able to redox cycle under physiological conditions, the cMyBP-C protein subunits, and the thin filament have been difficult to interrogate on a structural basis. Molecular dynamics simulations and advanced computational modeling presented in this work have located potential metal ion induced carbonylation hot spots on the C0 and C1 subunits and offer a reasonable hypothesis for the mechanism of interruption to thin filament binding. Future work can experimentally interrogate these suggested hot spots using advanced analytical techniques to identify carbonylated residues and to determine functional consequences. Interaction of Cu^{2+} or Fe^{2+} with selected amino acid residues and their impact on protein function can be further confirmed through targeted point mutations and functional studies with mutant proteins.

Author contributions

C.B., B.A, and A.R. designed research; C.B. performed research and analyzed data; C.B., B.A., and A.R. wrote the paper.

Declaration of competing interest

The authors declare that they have no known competing financial interests or personal relationships that could have appeared to influence the work reported in this paper.

Data availability

Ion occupancy grids and representative PDB files are deposited on GitHub: https://github.com/cbergonzo/cMyBP-C.

Acknowledgments

Certain commercial equipment, instruments, and materials are identified in this paper in order to specify the experimental procedure. Such identification does not imply recommendation or endorsement by the National Institute of Standards and Technology, nor does it imply that the material or equipment identified is necessarily the best available for the purpose. The views expressed in this article are those of the authors and do not necessarily reflect the official policy or position of the U.S. Food and Drug Administration and the Department of Health and Human Services, nor does mention of trade names, commercial products, or organizations imply endorsement by the U.S. Government. The authors declare no conflict of interest.

Appendix A. Supplementary data

Supplementary data to this article can be found online at https://doi.org/10.1016/j.jmgm.2023.108576.

References

[1] L. Carrier, G. Bonne, E. Bährend, B. Yu, P. Richard, F. Niel, B. Hainque, C. Cruaud, F. Gary, S. Labeit, J.B. Bouhour, O. Dubourg, M. Desnos, A.A. Hagège, R.J. Trent, M. Komajda, M. Fiszman, K. Schwartz, Organization and sequence of human cardiac myosin binding protein C gene (MYBPC3) and identification of mutations predicted to produce truncated proteins in familial hypertrophic cardiomyopathy, Circ. Res. 80 (1997) 427–434, https://doi.org/10.1161/01.RES.0000435859.24609.B3.

[2] B. Aryal, J. Jeong, V.A. Rao, Doxorubicin-induced carbonylation and degradation of cardiac myosin binding protein C promote cardiotoxicity, Proc. Natl. Acad. Sci. U. S. A. 111 (2014) 2011–2016, https://doi.org/10.1073/pnas.1321783111.

[3] S.L. Weng, K.Y. Huang, F.J. Kaunang, C.H. Huang, H.J. Kao, T.H. Chang, H. Y. Wang, J.J. Lu, T.Y. Lee, Investigation and identification of protein carbonylation sites based on position-specific amino acid composition and physicochemical features, BMC Bioinf. 18 (2017), https://doi.org/10.1186/s12859-017-1472-8.

[4] Y.J. Suzuki, M. Carini, D.A. Butterfield, Protein carbonylation, Antioxidants Redox Signal. 12 (2010) 323–325, https://doi.org/10.1089/ars.2009.2887.

[5] I. Dalle-Donne, G. Aldini, M. Carini, R. Colombo, R. Rossi, A. Milzani, Protein carbonylation, cellular dysfunction, and disease progression, J. Cell Mol. Med. 10 (2006) 389–406.

[6] L. Carrier, G. Mearini, K. Stathopoulou, F. Cuello, Cardiac myosin-binding protein C (MYBPC3) in cardiac pathophysiology HHS Public Access, Gene 573 (2015) 188–197, https://doi.org/10.1016/j.gene.2015.09.008.

[7] S. Ponnam, I. Sevrieva, Y.B. Sun, M. Irving, T. Kampourakis, Site-specific phosphorylation of myosin binding protein-C coordinates thin and thick filament activation in cardiac muscle, Proc. Natl. Acad. Sci. U. S. A. 116 (2019) 15485–15494, https://doi.org/10.1073/pnas.1903033116.

[8] S.C. Bardswell, F. Cuello, J.C. Kentish, M. Avkiran, CMyBP-C as a promiscuous substrate: phosphorylation by non-PKA kinases and its potential significance, J. Muscle Res. Cell Motil. 33 (2012) 53–60, https://doi.org/10.1007/s10974-011-9276-3.

[9] E. Maisonneuve, A. Ducret, P. Khoueiry, S. Lignon, S. Longhi, E. Talla, S. Dukan, Rules governing selective protein carbonylation, PLoS One 4 (2009), e7269, https://doi.org/10.1371/JOURNAL.PONE.0007269.

[10] D. Zhang, Z.C. Xu, W. Su, Y.H. Yang, H. Lv, H. Yang, H. Lin, iCarPS: a computational tool for identifying protein carbonylation sites by novel encoded features, Bioinformatics 37 (2021) 171–177, https://doi.org/10.1093/BIOINFORMATICS/BTAA702.

[11] H.-J. Kao, S.-L. Weng, K.-Y. Huang, F.J. Kaunang, J.B.-K. Hsu, C.-H. Huang, T.-Y. Lee, MDD-carb: a combinatorial model for the identification of protein carbonylation sites with substrate motifs, BMC Syst. Biol. 11 (2017) 137, https://doi.org/10.1186/s12918-017-0511-4.

[12] H. Lv, J. Han, J. Liu, J. Zheng, R. Liu, D. Zhong, CarSPred: a computational tool for predicting carbonylation sites of human proteins, PLoS One 9 (2014), 111478, https://doi.org/10.1371/JOURNAL.PONE.0111478.

[13] R.L. Chang, J.A. Stanley, M.C. Robinson, J.W. Sher, Z. Li, Y.A. Chan, A.R. Omdahl, R. Wattiez, A. Godzik, S. Matallana-Surget, Protein structure, amino acid composition and sequence determine proteome vulnerability to oxidation-induced damage, EMBO J. 39 (2020), https://doi.org/10.15252/EMBJ.2020104523.

[14] S.M. Idowu, M. Gautel, S.J. Perkins, M. Pfuhl, Structure, stability and dynamics of the central domain of cardiac myosin binding protein C (MyBP-C): implications for multidomain assembly and causes for cardiomyopathy, J. Mol. Biol. 329 (2003) 745–761, https://doi.org/10.1016/S0022-2836(03)00425-X.

[15] A. Ababou, M. Gautel, M. Pfuhl, Dissecting the N-terminal myosin binding site of human cardiac myosin-binding protein C: structure and myosin binding of domain C2, J. Biol. Chem. 282 (2007) 9204–9215, https://doi.org/10.1074/jbc.M610899200.
[16] A. Ababou, E. Rostkova, S. Mistry, C. Le Masurier, M. Gautel, M. Pfuhl, Myosin binding protein C positioned to play a key role in regulation of muscle contraction: structure and interactions of domain C1, J. Mol. Biol. 384 (2008) 615–630, https://doi.org/10.1016/j.jmb.2008.09.065.
[17] X.L. Zhang, S. De, L.P. McIntosh, M. Paetzel, Structural characterization of the C3 domain of cardiac myosin binding protein C and its hypertrophic cardiomyopathy-related R502W mutant, Biochemistry 53 (2014) 5332–5342, https://doi.org/10.1021/bi500784g.
[18] L. Govada, L. Carpenter, P.C.A. da Fonseca, J.R. Helliwell, P. Rizkallah, E. Flashman, N.E. Chayen, C. Redwood, J.M. Squire, Crystal structure of the C1 domain of cardiac myosin binding protein-C: implications for hypertrophic cardiomyopathy, J. Mol. Biol. 378 (2008) 387–397, https://doi.org/10.1016/j.jmb.2008.02.044.
[19] K.A. Michie, A.H. Kwan, C.S. Tung, J.M. Guss, J. Trewhella, A highly conserved yet flexible linker is part of a polymorphic protein-binding domain in myosin-binding protein C, Structure 24 (2016) 2000–2007, https://doi.org/10.1016/j.str.2016.08.018.
[20] J. Ratti, M. Gautel, M. Pfuhl, 3D NMR Structure of Domain cC0 of Cardiac Myosin Binding Protein C (MyBPC), To Be Publ, 2008. http://www.rcsb.org/pdb/explore/explore.do?structureId=2K1M.
[21] S.J. Fisher, J.R. Helliwell, S. Khurshid, L. Govada, C. Redwood, J.M. Squire, N. E. Chayen, An investigation into the protonation states of the C1 domain of cardiac myosin-binding protein C, Acta Crystallogr. Sect. D Biol. Crystallogr. 64 (2008) 658–664, https://doi.org/10.1107/S0907444908008792/FW5170SUP1.PDF.
[22] C. Risi, B. Belknap, E. Forgacs-Lonart, S.P. Harris, G.F. Schröder, H.D. White, V. E. Galkin, N-terminal domains of cardiac myosin binding protein C cooperatively activate the thin filament, Structure 26 (2018) 1604–1611, https://doi.org/10.1016/j.str.2018.08.007, e4.
[23] Y. Lu, A.H. Kwan, J. Trewhella, C.M. Jeffries, The C0C1 fragment of human cardiac myosin binding protein C has common binding determinants for both actin and myosin, J. Mol. Biol. 413 (2011) 908–913, https://doi.org/10.1016/j.jmb.2011.09.026.
[24] D.R. Roe, T.E. Cheatham 3rd, PTRAJ and CPPTRAJ: software for processing and analysis of molecular dynamics trajectory data, J. Chem. Theor. Comput. 9 (2013) 3084–3095, https://doi.org/10.1021/ct400341p.
[25] C. Tian, K. Kasavajhala, K.A.A. Belfon, L. Raguette, H. Huang, A.N. Migues, J. Bickel, Y. Wang, J. Pincay, Q. Wu, C. Simmerling, Ff19SB: amino-acid-specific protein backbone parameters trained against quantum mechanics energy surfaces in solution, J. Chem. Theor. Comput. 16 (2020) 528–552, https://doi.org/10.1021/acs.jctc.9b00591.
[26] H.J.C. Berendsen, J.R. Grigera, T.P. Straatsma, The missing term in effective pair potentials, J. Phys. Chem. 91 (1987) 6269–6271, https://doi.org/10.1021/j100308a038.
[27] P. Li, B.P. Roberts, D.K. Chakravorty, K.M. Merz, Rational design of particle mesh Ewald compatible Lennard-Jones parameters for +2 metal cations in explicit solvent, J. Chem. Theor. Comput. 9 (2013) 2733–2748, https://doi.org/10.1021/ct400146w.
[28] D.R. Roe, B.R. Brooks, A protocol for preparing explicitly solvated systems for stable molecular dynamics simulations, J. Chem. Phys. 153 (2020), 054123, https://doi.org/10.1063/5.0013849.
[29] C.W. Hopkins, S. Le Grand, R.C. Walker, A.E. Roitberg, Long time step molecular dynamics through hydrogen mass repartitioning, J. Chem. Theor. Comput. 11 (2015) 1864–1874, https://doi.org/10.1021/ct5010406.
[30] J.-P. Ryckaert, G. Ciccotti, H.J.C. Berendsen, Numerical integration of the cartesian equations of motion of a system with constraints: molecular dynamics of n-alkanes, J. Comput. Phys. 23 (1977) 327–341, https://doi.org/10.1016/0021-9991(77)90098-5.
[31] J. Åqvist, P. Wennerström, M. Nervall, S. Bjelic, B.O. Brandsdal, Molecular dynamics simulations of water and biomolecules with a Monte Carlo constant pressure algorithm, Chem. Phys. Lett. 384 (2004) 288–294, https://doi.org/10.1016/J.CPLETT.2003.12.039.
[32] R.J. Loncharich, B.R. Brooks, R.W. Pastor, Langevin dynamics of peptides: the frictional dependence of isomerization rates of N-acetylalanyl-N'-methylamide, Biopolymers 32 (1992) 523–535, https://doi.org/10.1002/bip.360320508.
[33] D.J. Sindhikara, S. Kim, A.F. Voter, A.E. Roitberg, Bad seeds sprout perilous dynamics: stochastic thermostat induced trajectory synchronization in biomolecules, J. Chem. Theor. Comput. 5 (2009) 1624–1631, https://doi.org/10.1021/ct800573m.
[34] T. Darden, D. York, L. Pedersen, Particle mesh Ewald: an Nlog(N) method for Ewald sums in large systems, J. Chem. Phys. 98 (1993) 10089–10092.
[35] R. Salomon-Ferrer, A.W. Götz, D. Poole, S. Le Grand, R.C. Walker, Routine microsecond molecular dynamics simulations with AMBER on GPUs. 2. Explicit solvent particle mesh Ewald, J. Chem. Theor. Comput. 9 (2013) 3878–3888, https://doi.org/10.1021/ct400314y.
[36] W.L. DeLano, The PyMOL Molecular Graphics System, 2002.
[37] W. Humphrey, A. Dalke, K. Schulten, VMD: visual molecular dynamics, J. Mol. Graph. 14 (1996) 33–38.
[38] F. Madeira, M. Pearce, A.R.N. Tivey, P. Basutkar, J. Lee, O. Edbali, N. Madhusoodanan, A. Kolesnikov, R. Lopez, Search and sequence analysis tools services from EMBL-EBI in 2022, Nucleic Acids Res. 50 (2022), https://doi.org/10.1093/NAR/GKAC240 gkac240–gkac240.
[39] X. Robert, P. Gouet, Deciphering key features in protein structures with the new ENDscript server, Nucleic Acids Res. 42 (2014) 320–324, https://doi.org/10.1093/nar/gku316.
[40] E.A. Permyakov, A.M.M. Gonçalves, Metal binding proteins, Encyclia 1 (2021) 261–292, https://doi.org/10.3390/ENCYCLOPEDIA1010024, 261-292. 1 (2021).
[41] I. Bertini, H.B. Gray, E.I. Stiefel, J.S. Valentine, Biological Inorganic Chemistry, First, University Science Boks, Sausalito, California, 2017.
[42] H. Lv, J. Han, J. Liu, J. Zheng, R. Liu, D. Zhong, CarSPred: a computational tool for predicting carbonylation sites of human proteins, PLoS One 9 (2014), e111478, https://doi.org/10.1371/JOURNAL.PONE.0111478.